

Article

Drop-Downs of an Outer Rotor Flywheel in Different Planetary Touch-Down Bearing Designs

Benedikt Schüßler *, Timo Hopf and Stephan Rinderknecht 

Institute for Mechatronic Systems, Technical University of Darmstadt, 64287 Darmstadt, Germany; timo.hopf@tu-darmstadt.de (T.H.); rinderknecht@ims.tu-darmstadt.de (S.R.)

* Correspondence: schuessler@ims.tu-darmstadt.de

Abstract: With an increase in renewable energy in the electricity grid, more storage capacity for grid stabilization and energy flexibilization is necessary. Dynamic grid stabilization is one possible application for flywheels. To increase the energy density of flywheels, they can be built as highly integrated outer rotor systems. The losses of the flywheel are reduced by magnetic levitation and operation under vacuum conditions. In the case of the failure or overload of the active magnetic bearings, the system needs touch-down bearings to prevent system destruction. Planetary touch-down bearings consisting of several small bearing units circumferentially distributed around the stator are especially suited for these systems. In the literature, these planetary touch-down bearings are rarely investigated, especially the number of bearing units. Therefore, this paper investigates the influence of the number of touch-down bearing elements in simulations and experiments for an 8-element and a 6-element touch-down bearing arrangement. For the investigation, drop-downs at four different speeds were performed. Simulation and experimental results showed that, for the 6-element touch-down bearing, in contrast to the 8-element touch-down bearing, maximal velocity did not increase with the drop-down speed. Therefore, the touch-down bearing arrangement with fewer elements is preferable.

Keywords: flywheel; energy storage; outer rotor; drop-down; touch-down bearing; backup bearing; catcher bearing; auxiliary bearing; vacuum



Citation: Schüßler, B.; Hopf, T.; Rinderknecht, S. Drop-Downs of an Outer Rotor Flywheel in Different Planetary Touch-Down Bearing Designs. *Actuators* **2022**, *11*, 30. <https://doi.org/10.3390/act11020030>

Academic Editors: Richard M. Stephan, Afonso Celso Del Nero Gomes and José Andrés Santisteban

Received: 27 December 2021

Accepted: 16 January 2022

Published: 21 January 2022

Publisher's Note: MDPI stays neutral with regard to jurisdictional claims in published maps and institutional affiliations.



Copyright: © 2022 by the authors. Licensee MDPI, Basel, Switzerland. This article is an open access article distributed under the terms and conditions of the Creative Commons Attribution (CC BY) license (<https://creativecommons.org/licenses/by/4.0/>).

1. Introduction

With an increase in renewable energy in the grid, more storage systems for grid stabilization and energy flexibilization are needed. One perfectly suited storage system is a hybrid energy storage system consisting of a lithium-ion battery and a flywheel. The advantages of the hybrid system compared to a stand-alone battery were shown in [1–3] for different use cases. To reduce losses, the flywheel is magnetically levitated and is operated under high vacuum conditions. Vertical levitation is realized with a permanent magnetic bearing, while the other directions are controlled with active magnetic bearings (AMB). A relevant topic for such a system is the behavior of the flywheel in case of an overload or malfunction of the AMB. To prevent destructive rotor–stator contact in the case of a drop-down, the system has planetary touch-down bearings (TDB) as described in [4] for other flywheels. Planetary TDB consist of several small bearing units that are circumferentially distributed around the stator. This TDB design has certain advantages compared to a conventional TDB consisting of one rolling element bearing. Two examples are the decoupling of the rotor diameter from the TDB diameter and the hindrance in the occurrence of a whirling motion. In general, whirling is more likely to occur for vertical rotors than for horizontal ones because the gravity force in horizontal systems has a whirl-suppressing effect, which was also shown in the literature for a planetary design with pins instead of rolling element bearings [5,6]. The planetary TDB design applied in the flywheel showed its capabilities to withstand multiple high speed drop-downs in an vertical

inner rotor test rig [7,8]. In [9], a high speed drop-down in a similar planetary TDB was shown. In the previously mentioned paper, the system was completely destroyed during a whirling motion initialized by an unstable AMB. During the drop-down, the AMB was still active. In comparison to that, this paper investigates the system behavior under complete AMB failure. There are several parameters influencing the drop-down behavior, such as stiffness, unbalance, friction, inertia and air gap size. In [4], some of these parameters were investigated in simulations, indicating that low friction and low unbalance are favorable. In [10], elastomer rings were investigated as damping elements to change the TDB stiffness. Results indicated that the service life of the TDB can be increased by a proper material and stiffness selection. A further parameter influencing the performance of the planetary TDB is the number of rolling element units in the planetary TDB. In the literature, the number of elements in the planetary TDB for outer rotor types has not been investigated yet. Therefore, this paper investigates the influence of the number of TDB elements. Figure 1 shows the structure of the planetary TDB for an 8- and 6-element TDB. The initial design of the test rig had a TDB with 8 TDB elements. Simulation results shown in Section 3.1 indicate that reducing the number of TDB elements leads to lower loads on the TDB. However, the number of TDB elements cannot be arbitrarily reduced. With the reduction in TDB elements, the difference between minimal and the maximal air gap increases due to the polygonal clearance. Figure 1 shows that the difference between maximal and minimal clearance is for the 8-element TDB was only 8.2%, while for the 6-element TDB, it increased to 15.5%. For a TDB with only four elements, the difference would increase to 41%. In a real system with production tolerances, this nonconstant clearance becomes even more relevant because tolerances further reduce the feasible air gap. For the investigated system, the second investigated number of TDB elements was set to 6 as a compromise between a reduction in TDB elements and feasible clearance.

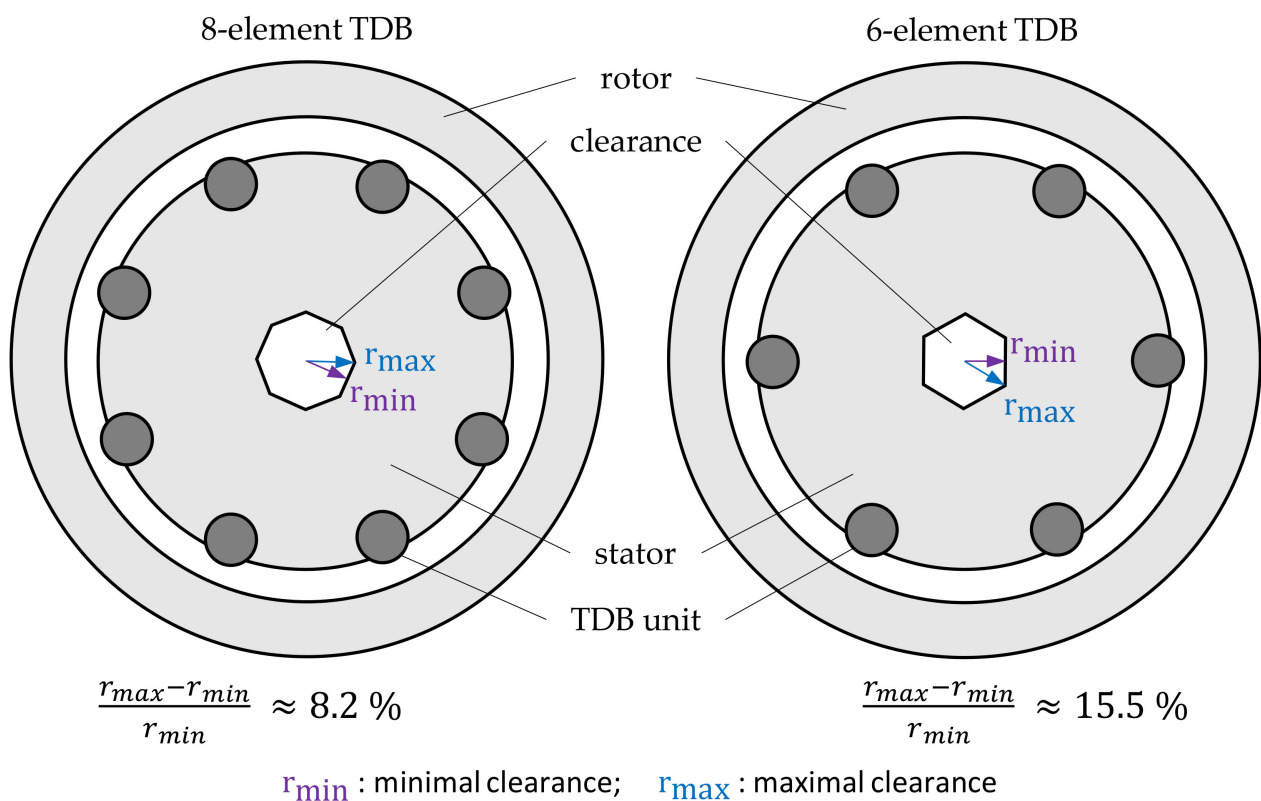


Figure 1. Designs of 8-element and 6-element planetary TDB with shape and difference in clearance (not to scale).

These two TDB designs (8- and 6-element TDB) were investigated and compared in simulations and experiments. During the performed drop-down test, the flywheel was

accelerated slightly faster than the target drop-down speed. After the flywheel had been accelerated, the inverter was switched off, and the flywheel slowly decelerated due to losses. When the target drop-down speed had been reached, the AMB for the radial direction were switched off. Consequently, the rotor started to spin down in the TDB.

2. Materials and Methods

2.1. Test Rig

Often, individual storage systems such as batteries or flywheels have specific disadvantages. In the case of batteries, a major disadvantage is calendrical and cyclic aging. For flywheels, it is the relatively low capacity. By combining two energy storage systems to one hybrid storage system, the overall usability of the systems can be increased because individual storage systems compensate the weaknesses of the other system. The hybrid energy storage system developed at the institute for mechatronic systems at TU Darmstadt is shown in Figure 2. It consisted of two components, battery and flywheel.

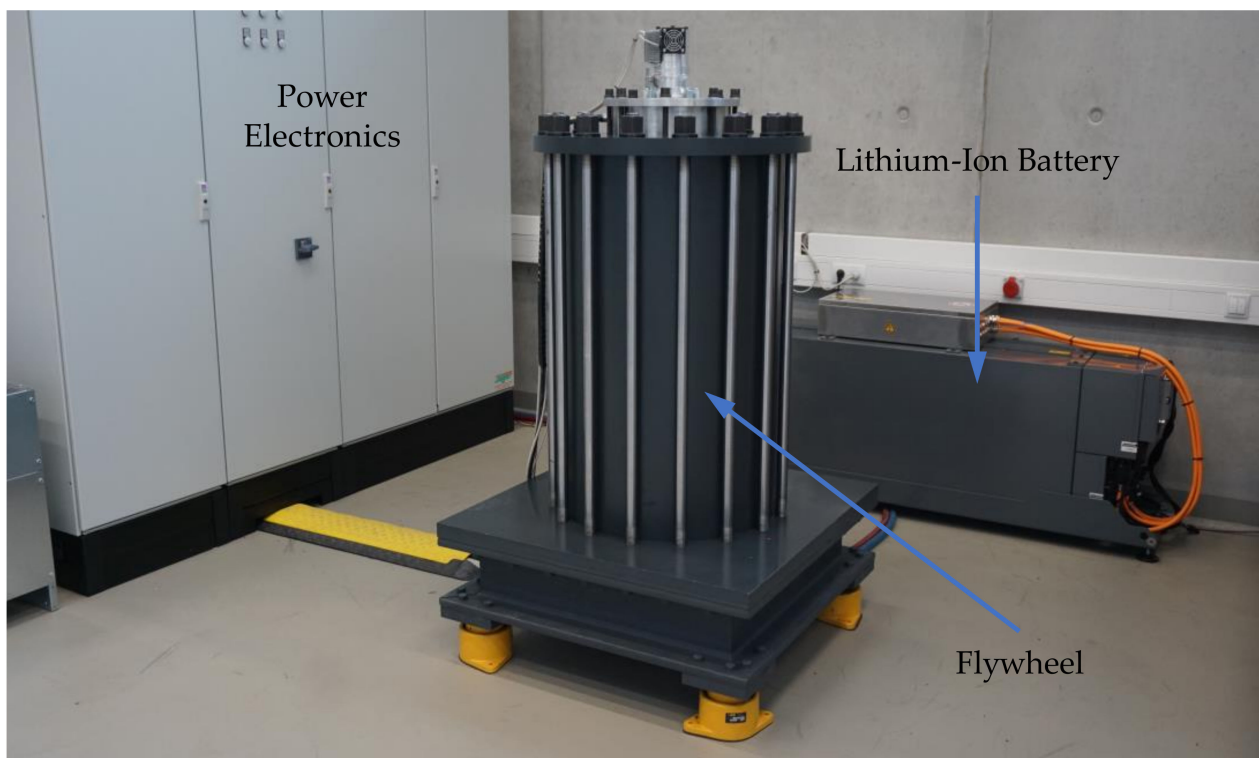


Figure 2. Hybrid energy storage system.

The electric wiring of the hybrid system is shown in Figure 3. Both storage systems are coupled to each other by a common DC link with 750 V. The DC link voltage is controlled by the grid inverter. The used power electronics were common industrial products. The grid inverter and motor inverter were from Bosch Rexroth, while the DC/DC converter for the battery was from Siemens. The motor inverter had two levels and a switching frequency of 12 kHz. If a malfunction occurred, the inverters were disabled, and the motor phases of the flywheel were connected to a braking resistor, so that the flywheel would decelerate. The hybrid energy storage was controlled by a programmable logic controller (PLC) in which different operational strategies were implemented. The PLC sent signals to the motor inverter or to the DC/DC inverter. The resulting change in DC link voltage was controlled by the grid inverter.

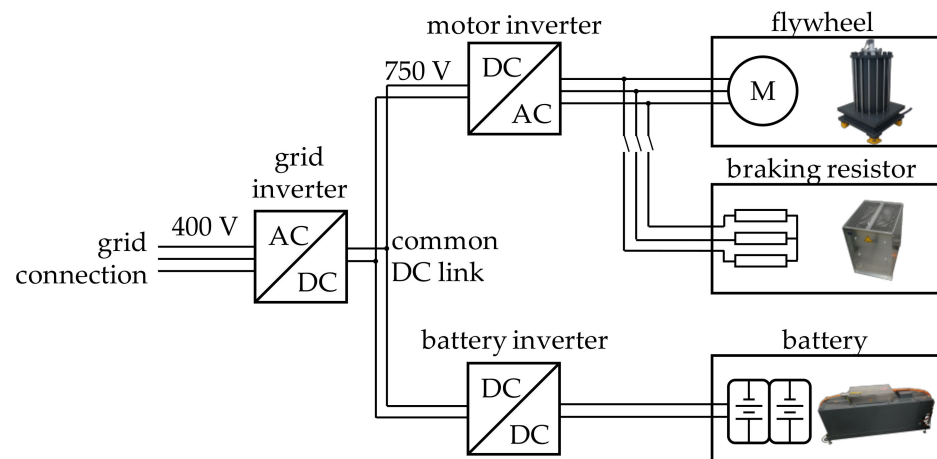


Figure 3. Electric wiring of hybrid energy storage system.

Individual storage systems in a hybrid system have different advantages. For the investigated system, the battery had high capacity, while the flywheel had high power. Specifications of the individual storage systems are given in Table 1. The battery was from Akasol. Cells in the battery were nickel manganese cobalt oxide (NMC). The flywheel was developed and built at the IMS of TU Darmstadt. Since flywheel SWIVT290 is highly relevant for the investigation of this paper, it is described in more detail in the following.

Table 1. Specification of individual storage systems of hybrid energy storage system. (a) Battery; (b) flywheel.

(a) Battery			(b) Flywheel		
Nominal power	73.5	kW	Max. power	100	kW
Max. voltage	605	V	Capacity	2.4	kWh
Min. voltage	389	V	Rotor mass	180	kg
Capacity	46	Ah	Outer rotor diameter	430	mm
Energetic capacity	24.5	kWh	Inner rotor diameter	290	mm
Mass	315	kg	Rotor length	850	mm
Cycle life (for 25 °C and 80% depth of discharge)	6800		Max. rotational speed	17,500	rpm

To operate the flywheel under vacuum conditions and for safety reasons, the flywheel was in steel containment. To increase the energy density of the flywheel, it was built as a hollow cylinder to achieve high inertia and it was produced from fiber-reinforced plastic (FRP) to reach high rotational speeds. Only functional inserts that were needed for the active components in the system and the raceways of the TDB were composed of metal. To reduce tangential stress due to rotation and enable high rotational speeds, inserts were segmented. This resulted in gaps between the segments under high rotational speeds. At the highest investigated drop-down speed, the gap between segments was less than 40 μm and therefore small compared to the radius of the rollers. Segments were glued to the FRP structure of the rotor. To reduce stress in the adhesive under high rotational speeds, only one-third of the surface of the segment was glued to the FRP structure. The remaining contacting surfaces of the segments and the FRP structure could slide. The structure of the flywheel is shown on the left in Figure 4. The core component of the system was the electrical machine, which was a permanent magnetic synchronous machine (PMSM) with five pole pairs. Above the electric machine, the passive axial magnetic bearing was placed. Permanent magnetic implementation has no need for power for axial levitation, which is an advantage that leads to high reliability and high efficiency. The next components are the AMB for the radial direction. They were built as differential winding with a focus of low losses in the rotor because it cannot be actively cooled. Due to vacuum, heat could only be

dissipated by radiation. The development of the radial AMB of the system is described in detail in [11]. Radial TDB were placed at the top and bottom. In the original configuration as is shown in Figure 4, the planetary system consisted of 8 bearing units. For a planetary TDB, clearance was not constant like for a conventional TDB, but was shaped as a polygon. Clearance boundaries are described by the herpolhodes of the rotor moving around the roller elements of the TDB. The nominal air gap was around 300 μm . To reduce wear, the surface of the rotor had higher hardness than that of the roller element surfaces of the TDB. In the bottom, the system had an axial TDB consisting of 4 rolling elements similar to the elements of the radial TDB. The contact surface for the axial TDB was the bottom surface of the rotor. For the other direction, there was no axial TDB but a simple end stop, since the rotor was not expected to move upwards against the gravity. To increase the stiffness of the stator, it was fixed at the bottom and top of the containment.

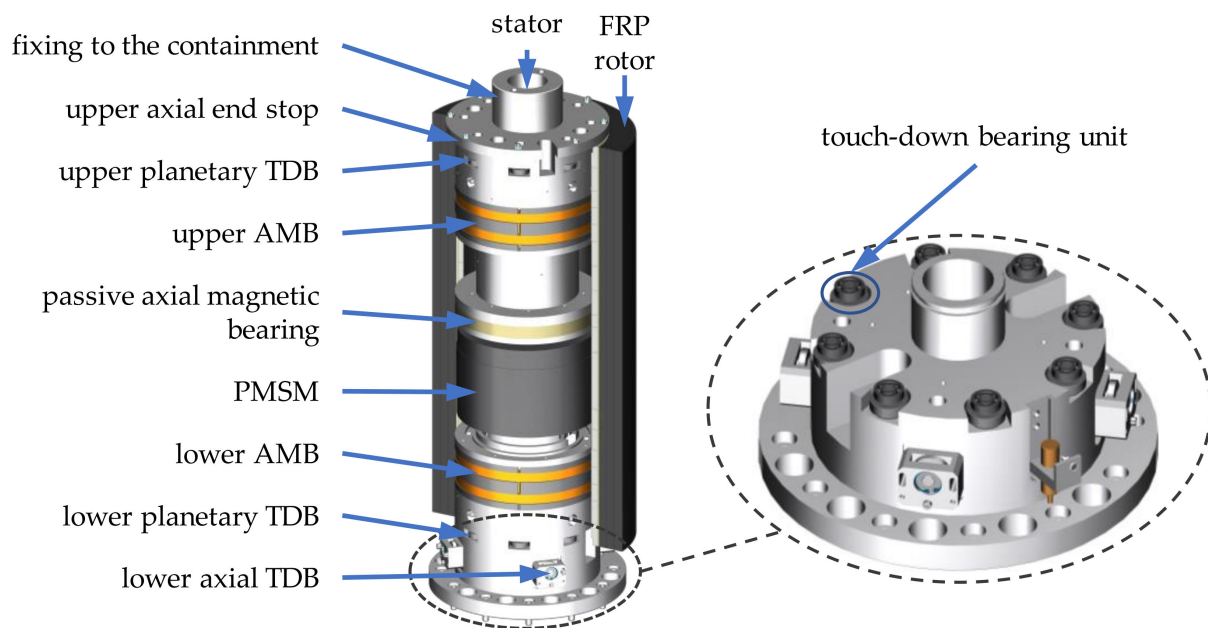


Figure 4. Partial section view of outer rotor flywheel SWIVT290 and section view of planetary TDB.

The amplifiers for the control of the radial AMB were industrial amplifiers from Mecatronix GmbH. For each AMB plane, a separate amplifier was used. The working voltage of the used amplifier was 48 V, and the maximal current per channel was ± 8 A with a frequency of 20 kHz. The control structure of the AMB was decentralized PID control, which was also implemented in the amplifier. Due to the high gyroscopy of the rotor and the changing air gap due to rotor enlargement under rotation, the control of the system was part of the research itself and is described in more detail in [12]. The rotor position that is needed for the control of the AMB was measured with type-BAW000W industrial inductive sensors from Balluff. For each AMB, four sensors were used, two for each direction. For the control, the difference of the two signals for one direction was used.

The system had various sensors, but for the drop-down investigation, only the previously described position and rotor-speed measurements were of interest. The rotational speed of the rotor was measured with a hall sensor that gave an impulse once per revolution. Since the system had high inertia, and rotational speed changed slowly, it was sufficient to only obtain a new signal once per rotation. For data acquisition, hardware and software from National Instruments were used. As a basis, an NI PXI-1033 real-time system was used with two PXI 6259 cards for the acquisition of positional and rotor-frequency data. Positional data were sampled with a sampling frequency of 10 kHz, while rotor-frequency data used a counter input.

2.2. Simulation Software

Drop-downs in TDB can be simulated with Analysis of Nonlinear Active Magnetic Bearing Systems (ANEAS) software, which was developed by Orth [13]. For the simulation, a flexible rotor and stator model were used. In the case of a contact, these two systems are coupled by nonlinear contact forces. Both for rotor and stator, finite-element (FE) models based on Timoshenko beams were built and are shown in Figure 5. The model of the rotor consisted of 13 nodes with 5 degrees of freedom per node: translation in both directions orthogonal to the rotation axis and the tilting around these directions, and the torsional degree of freedom. The yellow cross marks the center of gravity, red diamonds mark inputs such as forces in the TDB planes, and green diamonds mark outputs such as the rotor positions in the sensor planes. Because of the more complex geometry of the stator, its model had 22 nodes. However, each node had only 4 degrees of freedom, since the torsional degree of freedom was neglected. This was not needed, since the stator was not rotating; therefore, the unbalance did not need to be modeled. Furthermore, it was not expected that small rotations around the central axis would influence the drop-down behavior. Dark grey elements in the stator model in Figure 5 are mass elements without stiffness, and they were used to model the motor and active magnetic bearings, since the contribution to the stiffness of the overall system was low.

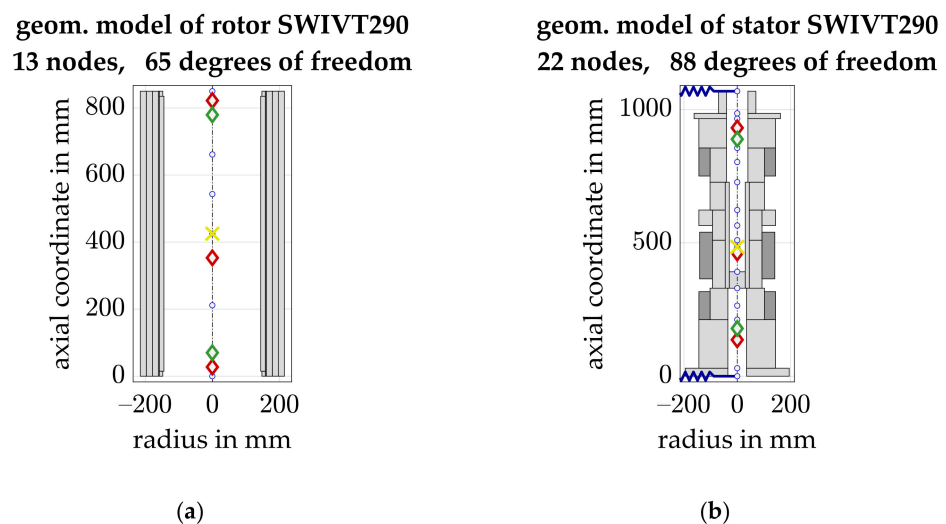


Figure 5. (a) FE rotor model; (b) FE stator model.

For the rotor, free–free bending frequencies resulting from the FE models, and the fixed–fixed bending frequencies for the stator are shown in Table 2. Due to the shape of the rotor, it had further eigenfrequencies in the range of bending frequencies such as warp frequencies, but they were not modeled in the FE model consisting of Timoshenko beams. To model these warp eigenfrequencies, a much more complex model is needed. In ANEAS, the FE rotor and stator models were modally reduced on the basis of Hankelsche singular values. The idea was to neglect not observable or not controllable states on the basis of the defined inputs and outputs of the model.

Table 2. Rotor and stator bending frequencies.

	Rotor Free–Free	Stator Fixed–Fixed
1. Bending frequency	736 Hz	117 Hz
2. Bending frequency	1078 Hz	257 Hz
3. Bending frequency	1597 Hz	435 Hz

Simulation environment ANEAS is mainly used to analyze inner rotor systems, and was only validated for drop-downs with inner rotor test rigs. However, there were only minor differences for outer and inner rotor systems in the modelling. One difference was the clearance boundary, which was defined by the herpolhodes of the rotor coming into contact with the bearing units of the TDB, and it is shown in Figure 6. In comparison to [8], the boundary of the clearance was no longer simplified to straight lines, but was implemented with the radius resulting from the kinematics. For an inner rotor system, the contacting surfaces were both concave; for an outer rotor type, one surface is concave while the other is convex. An inner rotor that moves, for example, to the left also touches the stator on the left side, but an outer rotor moving to the left touches the stator on the opposite side, so on the right. These differences were considered in the contact force calculation in the simulation. Another difference between inner and outer rotor systems that must mainly be considered for the interpretation of results is the whirling direction. For an inner rotor system, the direction of the friction-induced whirl is opposed to the rotation of the rotor, and thereby called backward whirl. For an outer rotor system, this changes. The friction leads to a whirling motion with the same direction as that of the rotor rotation. This fact is not specific for the planetary configuration of the TDB, but is also valid for outer rotor systems with conventional TDB. Therefore, this paper avoids the term backward whirl during the interpretation of results.

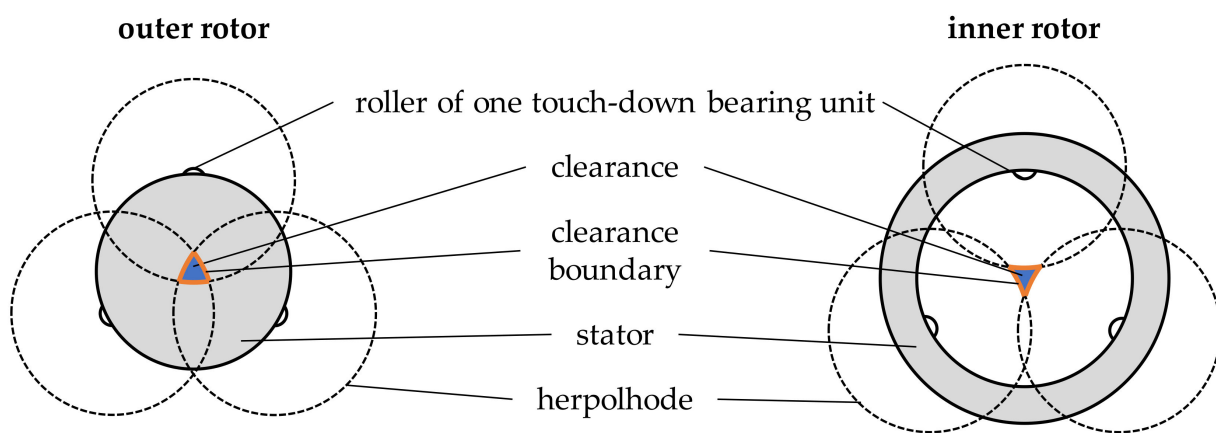


Figure 6. Clearance difference for outer and inner rotor types for a TDB with three elements.

The flexible rotor was coupled to the flexible stator by nonlinear contact forces on the basis of stiffnesses in the force flow. On the left side in Figure 7, the components considered for this stiffness are shown. One component was the contact stiffness of the rotor coming into contact with the roller of the TDB $k_{\text{roller,rotor}}$. This contact was considered to be a contact of two parallel cylinders. Due to tilting, there was a change from line to point contact between rotor and roller. Since the length of the rotor was much higher than the air gap size, the maximal tilting angle was less than 0.1° . Therefore, this change in contact area was neglected. For the relation between the deflection and contact force of two parallel cylinders, most of the literature gives a weak logarithmic relation, as is shown in the overviews of different models given in [14,15]. Therefore, this investigation applies a nonlinear model with a logarithmic relation instead of the linear model used in previous investigations with ANEAS. Some of the nonlinear models have the disadvantage of not being reasonable for large differences of diameter of the contacting cylinders since their primary application is to model the stiffness of joints where diameters are similar. However, in the planetary TDB, the rotor diameter was much larger than the roller diameter. Another disadvantage of some models is that they are not intended to model inner cylindrical contacts as they appear in the TDB between outer rotor and roller. The Goldsmith model given in [16] does not have these disadvantages and was thereby used for the investigation.

According to Goldsmith, the relation between contact force F and deflection δ for two parallel cylinders is calculated with Equation (1) [16].

$$\delta = \frac{F}{l_{\text{contact}} \pi E^*} \left(\ln \left(\frac{l_{\text{contact}} \pi E^* (R_{\text{rotor}} - R_{\text{roller}})}{F R_{\text{rotor}} R_{\text{roller}}} \right) + 1 \right) \text{ with } E^* = \frac{1}{\frac{1-\nu_{\text{rotor}}^2}{E_{\text{rotor}}} + \frac{1-\nu_{\text{roller}}^2}{E_{\text{roller}}}} \quad (1)$$

where ν and E express the Poisson ratio and the elastic modulus of the rotor and roller material, respectively. The length of the contact is expressed by l_{contact} . On the basis of this force–deflection relation, contact stiffness $k_{\text{roller,rotor}}$ was calculated. The second stiffness considered was bearing stiffness k_{bearing} . This nonlinear stiffness of the angular contact bearings was approximated by Equation (2), given in [17]. Stiffness depended on number of balls Z , mean diameter of bearing D_m and contact angle α_{bearing} of the angular contact bearing. Stiffness also depended on the compression of bearing \bar{x}_{bearing} itself, which was the reason for nonlinearity.

$$k_{\text{bearing}} = 3.312 \cdot 10^{10} Z \sqrt{D_m \left(\cos(\alpha_{\text{bearing}}) \right)^5 \bar{x}_{\text{bearing}}} \quad (2)$$

For overall static stiffness k_{stat} calculation, stiffnesses and their connections shown on the right in Figure 7 were used. The resulting overall static stiffness is given in Equation (3).

$$k_{\text{stat}} = \frac{2 k_{\text{bearing}} k_{\text{rotor,roller}}}{2 k_{\text{bearing}} + k_{\text{rotor,roller}}} \quad (3)$$

For deriving this equation, it was assumed that the force flow resulting from the contact was equally split to both bearings. This assumption was valid, since there was no axial force component expected resulting from the contact, and the tilting of the rotor was negligible, as described before.

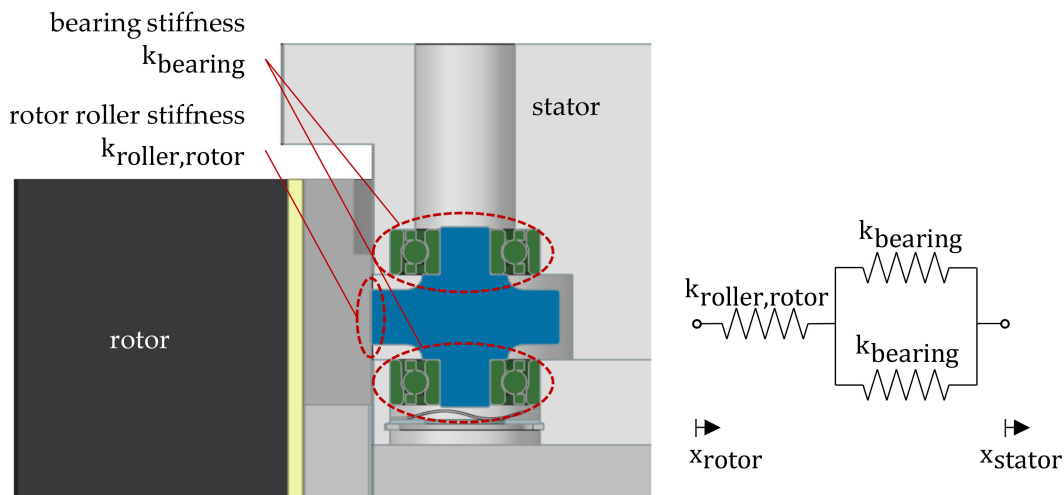


Figure 7. Stiffnesses considered in contact stiffness.

The inner damping of the rotor and stator was considered to be modal damping, while contact damping is based on the theory of Hunt and Crossley [18]. Therefore, contact force F_N shown in Equation (4) consisted of a static and a dynamic component. The static component was calculated with static stiffness k_{stat} and deflection δ . The dynamic component was proportional to static contact force F_{stat} and deflection velocity $\dot{\delta}$. Damping coefficient α was based on coefficient of restitution COR and initial contact velocity $\dot{\delta}^-$.

$$F_N = F_{\text{stat}} \left(1 + \alpha \dot{\delta} \right) \text{ with } \alpha = \frac{3(1 - \text{COR})}{2 \dot{\delta}^-} \text{ and } F_{\text{stat}} = k_{\text{stat}} \delta \quad (4)$$

This damping model was continuous and avoided negative contact forces for high and medium coefficients of restitution, as they are expected for steel–steel contacts. Since the rotor was axially levitated with a permanent magnetic bearing, and the electric machine had permanent magnets, the system had negative stiffness. This stiffness influenced the rotor behavior because it forced the rotor into one corner of the clearance. Stiffness was nonlinear because it was based on magnetic forces. However, the gap at the electric machine and the permanent magnetic bearing (1 mm) was much larger than the maximal clearance of the TDB, with around 0.35 mm in the corner of the clearance. Therefore, the change in the negative stiffness depending on the position of the rotor in the TDB was small. Thus, the negative stiffness was considered to be linearized to a value of -799 kN/m.

3. Results

3.1. Simulation Results

Simulations based on previously described models were conducted for the rotational drop-down speeds of the performed tests. The starting position was set to a value of 0.5% of the clearance. As described in [4], initial velocity and unbalance greatly influence the results. Therefore, the initial translational velocity was set to 0.015 m/s, which was the value derived from the initial velocity in the drop-down tests. The unbalance was set to 3.5 kg mm in both TDB planes, which was based on the unbalance orbit of the test rig at high rotational speeds. The value for the coefficient of restitution, which was used for the damping model of the contact force, was considered to be 0.75 for the simulation, which was in the range for COR values given in [19] for steel–steel contact.

On the basis of these parameters, we conducted simulations for the different rotational speeds and for the two different TDB designs. Since the drop-down at the highest speed was the most critical, these simulation results are exemplarily shown in Figure 8 for the 8-element TDB. The orbit given in Figure 8a shows that the rotor moved through the hole clearance, but was more often close to the boundaries of the clearance, which was due to the negative stiffness of the electric machine and the permanent magnetic axial bearing. Figure 8b shows the translational velocity of the rotor relative to the stator. The rotor started with low initial velocity, but gained velocity because of the high friction force due to the different surface speeds of the rollers and the rotor. After the rotor had accelerated all rollers at around 0.12 s, the rotor slowed down and may have stayed in one corner of the clearance. The first synchronization phase of the surface velocities was the most critical because the highest velocities and highest forces occurred. Velocity showed more peaks because, while the rotor stayed in one corner, the other rollers slowed down and had to be accelerated again when the rotor moved around in the TDB again. In other simulations with lower drop-down speeds, the rotor accelerated the rollers once and then stayed in one corner of the clearance for the rest of the simulation. For lower speeds, this can be explained by the shorter time of high tangential forces and faster synchronization. The high displacements visible in the orbit in Figure 8a are in the phase where the velocity of the rotor also reached its maximum.

Figure 9 shows the simulation results for the 6-element TDB. The orbit plot shows that the rotor moved around in the TDB less than with the 8-element TDB. After a jumping phase, the rotor stayed in one corner of the clearance. Therefore, in this case, the highest rotor velocity occurred in the first second after the drop-down, as is shown in Figure 9b. The difference was that the amplitude shown in Figure 9b was half of the amplitude with the 8-element TDB shown in Figure 8b. The highest drop-down speed was again reached at approximately 0.12 s. After 0.17 s, the rotor stayed in one corner of the clearance. The behavior of staying in one corner can be explained by the more acute angle of the clearance, and is in accordance to expectations.

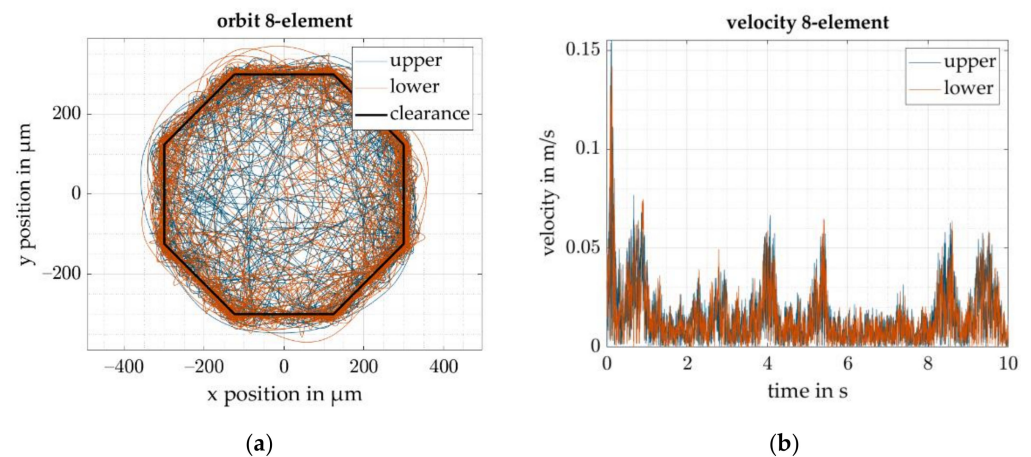


Figure 8. Simulation results for a 30 Hz drop-down in an 8-element TDB. (a) Rotor orbit; (b) rotor velocity.

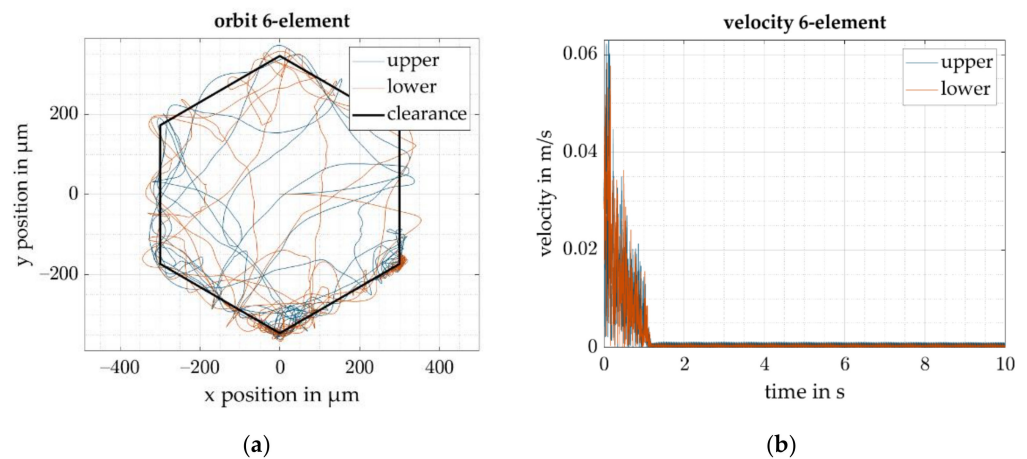


Figure 9. Simulation results for a 30 Hz drop-down in a 6-element TDB. (a) Rotor orbit; (b) rotor velocity.

To compare the severity of simulations for the different TDB designs and the different speeds, the maximal normal force can be used as severity indicator because, if the normal force on the bearing is much higher than its static load rating, one hit can destroy the bearing. Figure 10a shows the maximal normal force during the different simulations. For the 6-element TDB, the maximal normal forces changed only slightly with the drop-down frequency. Maximal normal force for the 6-element TDB (30 Hz) was less than 9% higher than for 3 Hz. For the 6-element TDB, forces were below 3200 N, resulting in less than 1600 N per bearing if the force flow was equally divided on both rolling element bearings in the TDB units. However, for the 8-element TDB design, normal forces increased with drop-down speed. For drop-down speed of 30 Hz, normal forces reached 5500 N, which resulted in 2750 N per bearing, but the static load rating was only 2100 N. As a result, simulations showed that a 6-element TDB was better-suited for the investigated system.

Since the force was not measured on the real system during the drop-down tests, it could not be used as a severity indicator. In [7], maximal translational velocity showed good coherence with the maximal force for a different test rig. Therefore, maximal translation velocity could be used as a severity indicator for drop-downs, which is not based on force values. Simulation results in this paper showed a similar trend for the maximal normal forces and maximal translational velocities for the investigated test rig. Figure 10b shows the maximal translational velocity of the rotor relative to the stator. For the 6-element TDB, it was nearly constant and varied by less than 8%, while it increased with the drop-down frequency for the 8-element TDB; therefore, it could be used as a severity indicator for analyzing the experimental results.

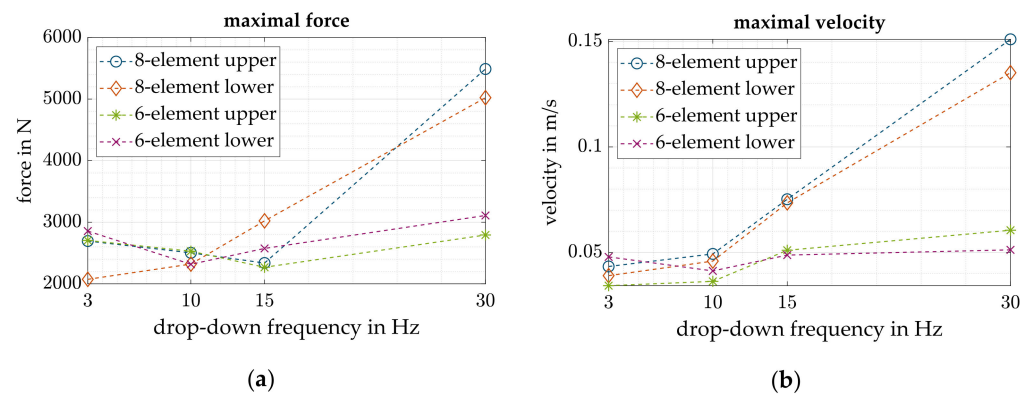


Figure 10. Comparison of simulation results for different TDB designs. (a) Maximal normal forces; (b) maximal velocity.

3.2. Experimental Results

Experimental testing was conducted with both TDB configurations. The drop-down speed was gradually increased until fast rotor movement occurred with the 8-element TDB. Therefore, drop-downs were performed for both configurations at 3, 10, 15, and 30 Hz. The testing procedure was to accelerate the flywheel to a slightly higher speed than the target drop-down speed and switch off the inverter, resulting in a slow deceleration. The rotational speed was monitored in the LabVIEW system based on hardware described in Section 2.1. As soon as the target drop-down speed had been reached, the AMB were manually switched off. Like in a real drop-down scenario of the flywheel, tests were performed under high vacuum conditions. After the AMB were disabled the motor phases were switched to a braking resistor automatically. As a result of the rotor movement and the permanent magnets of the electric machine, a current was induced in the motor windings leading to a damping effect. This damping effect was not modeled in the simulation. However, forces resulting from this effect were expected to be much lower than other forces during the drop-down. After the tests had been performed with the 8-element TDB, the flywheel was disassembled and changed into the 6-element TDB. Bearings in the 8-element configuration were hybrid spindle bearings of type 6001 with a MoS₂ lubrication. For the 6-element configuration, bearings were changed into hybrid spindle bearings of type 6200 with 550 N higher load capacity, which was according to simulations needed for higher drop-down speeds. Lubrication was changed to more persistent lubrication. Vacuum grease (Krytox AB240) was used, which showed good performance in tests with the TDB test rig [7].

For the evaluation of the drop-downs, the position signal was used. The position was measured in the sensor plane, but the rotor movement was restricted by the TDB. Therefore, the position in the TDB plane was calculated by assuming a rigid rotor. For the evaluation, the translational velocity of the rotor was calculated by differentiating the position signal because the velocity was not directly measured. Since the position signal was measured by a real sensor, it contained noise and errors due to the segmented rotor. To reduce the enlargement of these errors by differentiation, the position signal was filtered with a 500 Hz low pass filter (LP). Loads on the TDB may increase with an increasing drop-down speed. Therefore, the drop-down at a rotor speed of 30 Hz was analyzed. Figure 11 shows the experimental results for 10 s for the drop-down at 30 Hz for the 8-element TDB. Figure 11a shows that the rotor had no continuous contact to the TDB most of the time, and thereby had a jumping movement in which it rarely moved through the center of the clearance. The orbit also shows that there was a phase when the rotor moved around on a nearly circular path in the TDB without losing contact. The path was nearly circular instead of polygonal because of the deformation of the TDB due to the contact force. During this synchronization phase, displacements were higher than those the rest of the time, resulting in high loads on the TDB. The velocity diagram in Figure 11b shows a peak around 0.8 s, which was at the time at which the rotor was moving without losing contact. After the

TDB units had rapidly accelerated and had the same surface velocity as the rotor, the rotor movement again changed into noncontinuous contact movement. Figure 11 also shows that the movement of the rotor was similar for both TDB planes. The orbit in Figure 11a shows that the TDB were not perfectly aligned due to manufacturing tolerances: there was a misalignment in the x direction. Figure 11b shows that the velocity of the rotor during the jumping phases was slightly higher in the upper bearing.

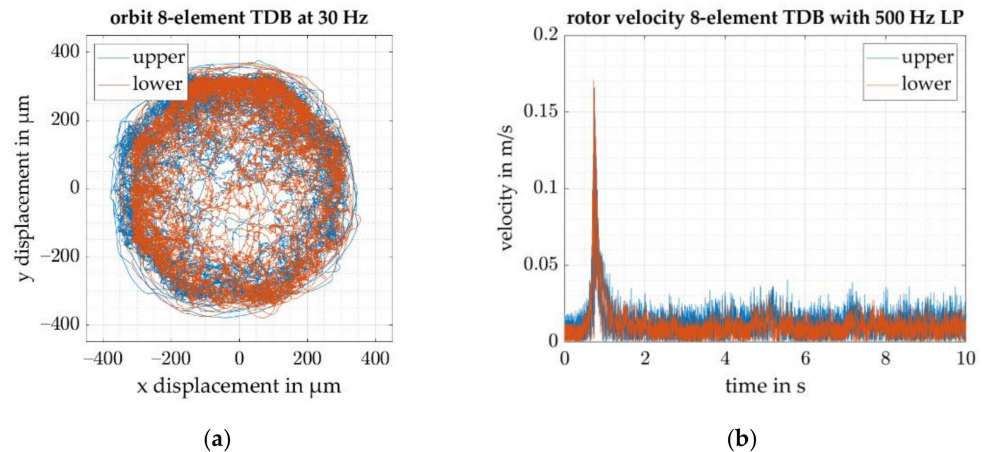


Figure 11. Experimental results for a 30 Hz drop-down in an 8-element TDB. (a) Rotor orbit: (b) rotor velocity.

Compared to the simulation results, both simulations and experiments showed that the rotor had a phase in which it performed a circular movement in the TDB, which is shown in both the orbit plot and the velocity plot. The difference is that the phase with the high velocities started later and had a longer duration in the experiments. In addition, the amplitude of the maximal velocity was higher in the experiments. However, even when the signal had been filtered for analysis, the absolute values were still influenced by noise, which also occurred below the cutoff frequency.

Figure 12 shows the experimental results for the 6-element TDB for a rotor drop-down at 30 Hz. Compared to the orbit plot from Figure 11a, the rotor movement in Figure 12a showed, during the whole drop-down time, a jumping characteristic with the tendency to stay in one corner of the clearance. Therefore, there was no dominant peak in the velocity. However, at around 1.5, 6, and 8.1 s, the velocity had a value around double that at other times. In the velocity plot in Figure 11b, there were similar regions with increased velocity, but due to the peak at 0.8 s during synchronization, they were not as dominant as those in Figure 12b. Again, the velocity in the upper bearing was slightly higher. Figure 12a also shows that there was some difference in the geometry of the clearance of the two TDB, which was again due to manufacturing tolerances. The moving direction of the rotor at the beginning of the drop-downs was the same in all experiments. In the upper TDB, the rotor moves to the positive x and negative y directions, while it moved in the lower TDB to the positive x and positive y directions. This can be explained by a difference between the geometric center and magnetic center of the electric machine and the passive axial magnetic bearing, which was again due to manufacturing tolerances. A comparison of these experimental results from Figure 12 and the simulation results from Figure 9 show that the rotor movement in the experiments was higher. It still tended to stay in one corner, but it was not as clearly visible as that in Figure 9. This can be explained by the idealized assumptions for the contacting surfaces. The gaps that may occur between the different segments of the races were not considered in the simulation. Imperfections in the surfaces resulting from, for example, adhesion from previous contacts or due to manufacturing, were not considered in the simulation. Both idealized assumptions lead to smoother behavior in the simulations.

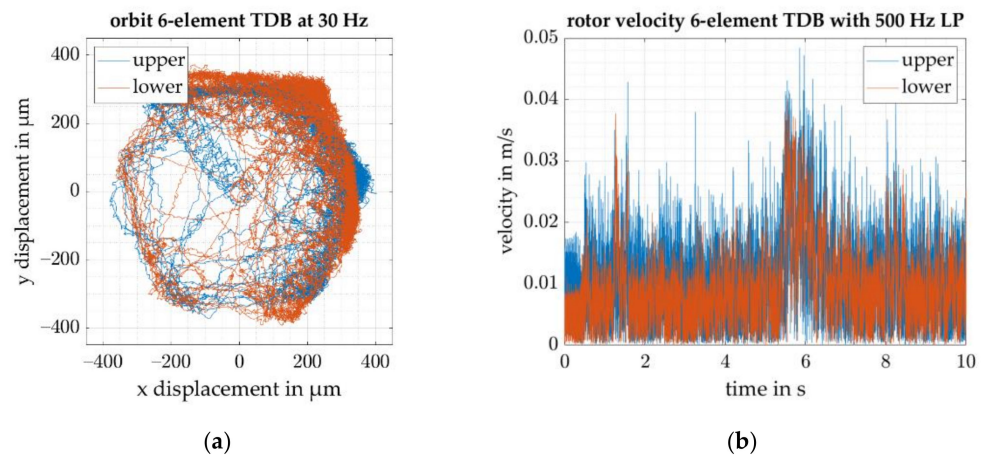


Figure 12. Experimental results for a 30 Hz drop-down in a 6-element touch-down bearing. (a) Rotor orbit; (b) rotor velocity.

The severity of the drop-downs could be evaluated on the basis of different severity indicators. As described before, the maximal translational velocity can be used as a severity indicator due to the high coherence to the maximal forces, and the fact that it could be calculated from position data. The maximal velocity is shown in Figure 13 for the different experiments. For the 6-element TDB, maximal velocity was lower than that for the 8-element TDB. The highest difference was seen in the maximal velocity for a drop-down speed of 30 Hz, where the maximal velocity was only around 0.05 m/s instead of around 0.18 m/s, which resulted in much lower peak loads for the bearings. Therefore, the loads for the TDB were much lower with 6 elements. Compared to the simulation results shown in Figure 10, the general behavior was the same. For the 6-element TDB, there was nearly no change in maximal velocity, while it increased for the 8-element TDB. However, the absolute values were higher for the experiments, especially for high drop-down speeds. This could be explained by the previously discussed idealized assumptions.

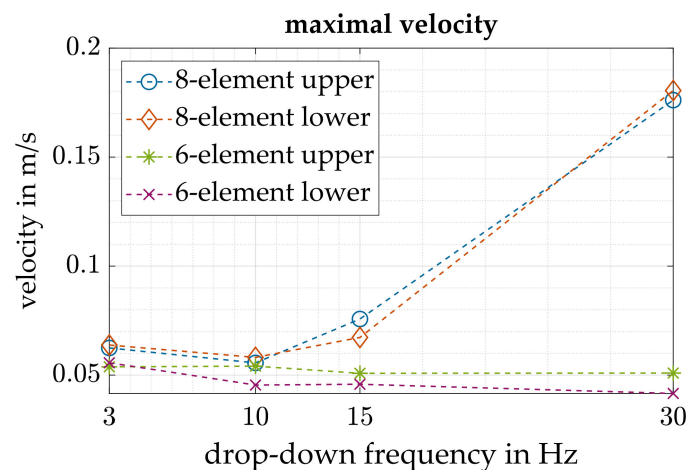


Figure 13. Experimental result comparison of maximal velocity for different TDB designs.

After the drop-down tests with the 6-element TDB, the test rig was disassembled again to see if there was any damage to the components. There was no visible damage to stator or rotor components. Figure 14 shows the raceway of the upper TDB of the rotor. The dark track was just plaque that could easily be removed. The underlying surface was not damaged. Figure 14 also shows the segmented raceway for the TDB of the rotor. Since the rotor was ground after the 20 segments had been fixed to the rotor with an adhesive, there was no difference in height between segments.

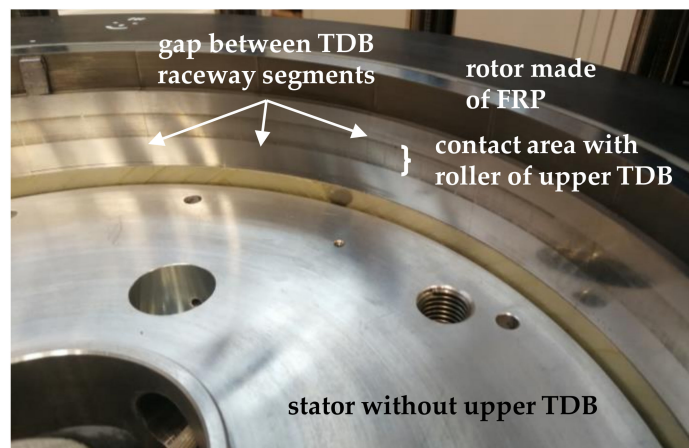


Figure 14. Raceways of the TDB of the test rig after drop-down tests.

When rotating the bearings, there was no noticeable damage to the rolling element bearings. Figure 15 shows the TDB after the drop-downs. Figure 15a shows the 8-element TDB, and Figure 15b shows the 6-element TDB. On both TDB configurations, there was no damage to the roller element. This could be explained by the low number of drop-downs and the relatively low drop-down speed. The maximal rotational speed of the flywheel was 18,000 rpm. Therefore, the investigated maximal drop-down speed was only 10% of the maximal speed. However, even with these relatively slow drop-down speeds, the different behavior of the TDB could be demonstrated.

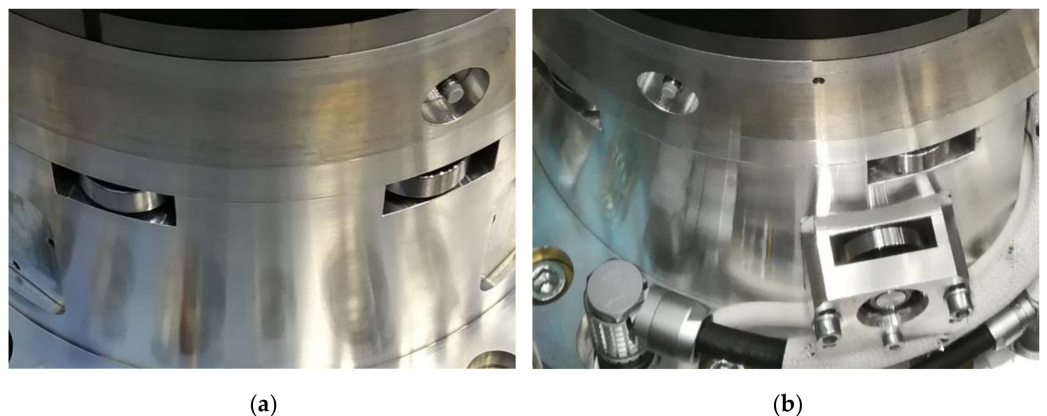


Figure 15. Picture of the lower TDB after the drop-down tests; (a) 8-element TDB; (b) 8-element TDB with axial TDB mounted below.

4. Conclusions

Two different planetary TDB designs for outer rotor flywheels were investigated in simulations and experiments on the SWIVT290 prototype. First, the structure of the flywheel was described. Afterwards, simulations and used models were presented. The results of the simulations showed that, for the 6-element TDB, the maximal force during the drop-downs was nearly independent of the drop-down frequency. However, for the 8-element TDB, maximal force increased with the drop-down speed, and the reached simulation values were higher than those of the static load rating of the bearings; therefore, this may destroy them. Since force was not measured during the tests, maximal velocity was introduced as a severity indicator because it showed a similar trend as that of the maximal force, but could only be calculated from the position signal. Experimental results showed a similar trend as that of the simulations even if the absolute values of the maximal velocity vary. This could be explained by imperfections on the rotor raceways due to manufacturing, previous contacts, or gaps between the segments under rotation. The influence of these imperfections on

bearing loads must be further analyzed. Both simulations and experimental results showed that the maximal velocities in the 6-element TDB were lower than those in the 8-element TDB, leading to the conclusion that maximal loads in the 6-element TDB were also lower than those in the 8-element TDB. Therefore, the 6-element TDB design was preferred for the shown outer-rotor flywheel system. The better performance of the 6-element TDB must be validated for higher speed levels. The influence of the number of elements in the TDB will also be investigated for other test rigs, since the ideal number of elements is influenced by other parameters such as the stiffness of the test rig or the TDB elements themselves. With the test rig used in this investigation, the number of TDB elements could not be further reduced without the danger of rotor–stator contact elsewhere than in the TDB. To investigate the possibility of further improvements with a lower number of TDB elements, a different test rig or a revision of the current test rig is necessary. However, from this investigation, it could be concluded that the simulation can be used in principle to investigate the behavior of the system with a varying number of TDB elements.

Author Contributions: Conceptualization, B.S.; formal analysis, B.S.; investigation, B.S. and T.H.; methodology, B.S.; software, B.S.; supervision, S.R.; visualization, B.S.; writing—original draft, B.S.; writing—review and editing, B.S. All authors have read and agreed to the published version of the manuscript.

Funding: Results were obtained within project “Elektrische Energiespeicher zur Netzstabilisierung—Schwungmassenspeicher in Außenläuferbauform” with grant number 03ET6064A, which is funded by the Federal Ministry for Economic Affairs and Energy on the basis of a decision by the German Bundestag.

Institutional Review Board Statement: Not applicable.

Informed Consent Statement: Not applicable.

Data Availability Statement: The data presented in this study are available on request from the corresponding author.

Acknowledgments: We acknowledge support by the Deutsche Forschungsgemeinschaft (DFG, German Research Foundation) and the Open Access Publishing Fund of Technical University of Darmstadt.

Conflicts of Interest: The authors declare no conflict of interest.

References

1. Mouratidis, P.; Schneider, M.; Genov, I.V.; Rinderknecht, S. Hybrider Energiespeicher-Prüfstand mit kombiniertem kinetischem und elektrochemischem Energiespeicher. In Proceedings of the Fachtagung Mechatronik 2019, Paderborn, Germany, 27–28 March 2019.
2. Mouratidis, P.; Schüßler, B.; Rinderknecht, S. Hybrid Energy Storage System consisting of a Flywheel and a Lithium-ion Battery for the Provision of Primary Control Reserve. In Proceedings of the 2019 8th International Conference on Renewable Energy Research and Applications (ICRERA), Brasov, Romania, 3–6 November 2019; pp. 94–98, ISBN 978-1-7281-3587-8.
3. Weitzel, T.; Schneider, M.; Franke, G.; Glock, C.; Rinderknecht, S. Sizing and Operating a Hybrid Electric Energy Storage System Using Meta Heuristics. In Proceedings of the 8th International Conference & Workshop—Quest for Energy, Venice, Italy, 29–31 May 2018.
4. Quurck, L.; Franz, D.; Schüßler, B.; Rinderknecht, S. Planetary backup bearings for high speed applications and service life estimation methodology. *Mech. Eng. J.* **2017**, *4*, 17-00010. [[CrossRef](#)]
5. Lahiri, S.; Santos, I.F. Experimental quantification of dynamic forces and shaft motion in two different types of backup bearings under several contact conditions. *Mech. Syst. Signal Processing* **2013**, *40*, 301–321. [[CrossRef](#)]
6. Lahiri, S.; Santos, I.F.; Weber, H.I.; Hartmann, H. On The Nonlinear Dynamics of Two Types of Backup Bearings—Theoretical and Experimental Aspects. *J. Eng. Gas Turbines Power* **2012**, *134*, 112503. [[CrossRef](#)]
7. Quurck, L.; Viitala, R.; Franz, D.; Rinderknecht, S. Planetary Backup Bearings for Flywheel Applications. In Proceedings of the International Symposium on Magnetic Bearings, Beijing, China, 13–17 August 2018.
8. Quurck, L. *Fanglagerung Magnetgelagerter Schwungmassenspeicher*; Tuprints: Darmstadt, Germany, 2019.
9. Schüßler, B.; Hopf, T.; Franz, D.; Schneider, M.; Rinderknecht, S. High Speed Drop Down in a Planetary Touch-Down Bearing of an Outer Rotor Flywheel System. In Proceedings of the 14th International Conference on Dynamics of Rotating Machines, Gdańsk, Poland, 17–19 February 2021; pp. 166–174, ISBN 978-83-88237-98-0.

10. Schüßler, B.; Hopf, T.; Rinderknecht, S. Simulative investigation of rubber damper elements for planetary touch-down bearings. *Bull. Pol. Acad. Sci. Tech. Sci.* **2021**, e139615. [[CrossRef](#)]
11. Franz, D.; Richter, M.; Schneider, M.; Rinderknecht, S. Homopolar Active Magnetic Bearing Design for Outer Rotor Kinetic Energy Storages. In Proceedings of the 2019 IEEE International Electric Machines & Drives Conference (IEMDC), San Diego, CA, USA, 12–15 May 2019; pp. 774–778, ISBN 978-1-5386-9350-6.
12. Hopf, T.; Richter, M.; Schüßler, B.; Rinderknecht, S. Diametral Enlargement of Highly Gyroscopic Outer-Rotors in Active Magnetic Bearings. In Proceedings of the 17th International Symposium on Magnetic Bearings, Virtual, Rio de Janeiro, Brazil, 18–21 August 2021; pp. 240–254.
13. Orth, M.; Nordmann, R. ANEAS: A Modeling Tool for Nonlinear Analysis of Active Magnetic Bearing Systems. *IFAC Proc. Vol.* **2002**, *35*, 811–816. [[CrossRef](#)]
14. Pereira, C.M.; Ramalho, A.L.; Ambrósio, J.A. A critical overview of internal and external cylinder contact force models. *Nonlinear Dyn.* **2011**, *63*, 681–697. [[CrossRef](#)]
15. Skrinjar, L.; Slavič, J.; Boltežar, M. A review of continuous contact-force models in multibody dynamics. *Int. J. Mech. Sci.* **2018**, *145*, 171–187. [[CrossRef](#)]
16. Goldsmith, W. *Impact: The Theory and Physical Behaviour of Colliding Solids*; Edward Arnold: London, UK, 1960.
17. Gargiulo, E.P., Jr. A simple way to estimate bearing stiffness. *Mach. Des.* **1980**, *52*, 107–110.
18. Hunt, K.H.; Crossley, F.R.E. Coefficient of Restitution Interpreted as Damping in Vibroimpact. *J. Appl. Mech.* **1975**, *42*, 440. [[CrossRef](#)]
19. Marinack, M.C.; Musgrave, R.E.; Higgs, C.F. Experimental Investigations on the Coefficient of Restitution of Single Particles. *Tribol. Trans.* **2013**, *56*, 572–580. [[CrossRef](#)]